Characterizing the radiative effect of rain using a global ensemble of cloud resolving simulations

Journal of Advances in Modeling Earth Systems

RESEARCH ARTICLE
10.1029/2018MS001415

Characterizing the Radiative Effect of Rain Using a Global Ensemble of Cloud Resolving Simulations

P. G. Hill[1], J. C. Chiu[1,2], R. P. Allan[1,3], and J.-D. Chern[4,5]

[1]Department of Meteorology, University of Reading, Reading, UK, [2]Department of Atmospheric Science, Colorado State University, Fort Collins, CO, USA, [3]National Centre for Earth Observation, Reading, UK, [4]NASA Goddard Space Flight Center, Greenbelt, MD, USA, [5]Earth System Science Interdisciplinary Center, University of Maryland, College Park, MD, USA

Key Points:
- We provide the first global assessment of the radiative effect of rain
- In the global mean, the radiative effect of rain is negligibly small
- At smaller spatial scales and shorter timescales, rain radiative effects exceeding 10 W m^{-2} do occur, but infrequently

Correspondence to:
P. G. Hill,
p.g.hill@reading.ac.uk

Citation:
Hill, P. G., Chiu, J. C., Allan, R. P., & Chern, J.-D. (2018). Characterizing the radiative effect of rain using a global ensemble of cloud resolving simulations. *Journal of Advances in Modeling Earth Systems*, *10*. https://doi.org/10.1029/2018MS001415

Received 25 JUN 2018
Accepted 1 OCT 2018
Accepted article online 4 OCT 2018

Abstract The effect of rain on radiative fluxes and heating rates is a process that is neglected in most of the large scale atmospheric models used for weather forecasting or climate prediction. Yet to our knowledge, the magnitude of the resulting radiative bias remains unquantified. This study aims to quantify the rain radiative effect (RRE) at a range of temporal and spatial scales, as a step toward determining whether the radiation schemes in these models should include rain. Using off-line radiative transfer calculations with input from an ensemble of cloud resolving model simulations, we find that rain has a negligible effect on global mean radiative fluxes (less than 0.2 W m^{-2}). Weekly mean RREs at specific locations may be larger (less than 4 W m^{-2}). At the finest temporal and spatial resolutions, the RRE can occasionally be much larger again (greater than 100 W m^{-2}), but values exceeding 10 W m^{-2} occur in less than 0.1% of cases. Using detailed analysis of case studies we demonstrate that the magnitude and direction of the RRE depend on the rain water path, its vertical location with respect to cloud, and, for longwave radiation, the temperature at which it occurs. Large RREs generally only occur when the rain water path is large and the cloud water path is small. These cases are infrequent and intermittent. As the RREs are generally small, we conclude that this missing process is unlikely to be important for large scale atmospheric models.

1. Introduction

Accurate simulation of the atmospheric radiation budget is crucial for modeling both the general circulation and the effect of anthropogenic emissions on climate. Nevertheless, comparison with satellite and surface irradiance observations shows that many large scale atmospheric models (LSAMs) have persistent large shortwave (SW) and longwave (LW) radiation errors, with typical zonal mean errors of 10 W m^{-2} at the top of atmosphere (TOA; e.g., Calisto et al., 2014; Dolinar et al., 2014), and typical global mean errors of 10 W m^{-2} at the surface (e.g., Ma et al., 2014; Wild et al., 2014). Most of these errors are thought to be due to deficiencies in modeled cloud and aerosol, but errors can also result from neglecting physical processes in the radiation schemes. One particular bias that persists in many LSAM radiation schemes is to neglect the radiative impacts of precipitating hydrometeors, including snow, rain, hail, and graupel. Li et al. (2013) hypothesized that this may be partly responsible for the particularly large (greater than 20 W m^{-2}) climate model radiation biases that are evident in strongly precipitating regions.

However, on a global scale, the magnitude of the radiative effect of precipitating hydrometeors remains uncertain. It is certainly smaller than that of suspended hydrometeors (i.e., clouds), because precipitating hydrometeors occur less frequently and (as precipitating particles are larger) cause less extinction per unit mass than suspended hydrometeors. Yet the primary reason that the radiative effects of precipitating hydrometeors are not accounted for in LSAMs is that historically, they have not been treated explicitly by the microphysics and consequently their mass mixing ratios have not been available for input to the radiation schemes. However, cloud resolving models (CRMs), which explicitly represent the microphysics of precipitating hydrometeors, usually also account for their radiative effects (e.g., Fu et al., 1995; Jiang & Cotton, 2000; Petch, 1998; Phillips & Donner, 2006; Tao et al., 2014). Moreover, there is a growing body of evidence to suggest that neglecting precipitating ice (snow) in radiative transfer calculations may lead to nonnegligible biases in LSAMs (e.g., Chen et al., 2018; Li, Forbes, et al., 2014; Li, Lee, et al., 2014; Li, Lee, Waliser, et al., 2016; Li, Lee, Yu, et al., 2016). As a result, Li, Waliser, et al. (2016) suggested that the persistent radiation biases seen across many LSAMs may partly result from neglecting the radiative effects of precipitating hydrometeors.

Compared to snow (e.g., Waliser et al., 2011), the radiative impacts of neglecting rain are less well documented. Previous assessments of the radiative effect of rain are rare and have been based on a limited number of test cases with some contradictory conclusions. Based on radiative transfer calculations for a two-dimensional CRM simulation of 24 hr of a tropical mesoscale convective system, Xu and Randall (1995) found that the impact of rain on the SW transmission and albedo was less than 0.002 and concluded that the radiative effects of rain were negligible. In contrast, based on idealized cloud and rain profiles, Savijärvi et al. (1997) found that rain increased the total column SW absorption by approximately 10% for a heavily precipitating cumulonimbus with rain drops present throughout the depth of the cloud. Moreover, Savijärvi and Räisänen (1998) found that for an optically thick cloud with base at 3 km, including rain below the cloud base in their radiative transfer calculations could increase the downwelling LW irradiance at the surface by up to 24 W m^{-2}. However, they acknowledged that in reality the mean effect was likely to be much smaller due to larger water vapor values below cloud base than in their calculations. To our knowledge, these are the only existing attempts to quantify the broadband radiative effect of rain; the global radiative effect of rain remains unquantified.

The aim of this study is thus to advance upon this limited but potentially important past research by calculating the rain radiative effect (RRE) for a realistic set of atmospheric profiles encompassing the whole globe. Using these calculations, we aim to quantify and explain the direct radiative effects of rain across a range of temporal and spatial scales. This is necessary to determine whether including rain in LSAM radiative transfer calculations warrants further investigation. Our estimate of the RRE is based on detailed radiative transfer calculations using the SOCRATES (Suite Of Community RAdiative Transfer codes based on Edwards & Slingo, 1996) radiation scheme and a global ensemble of CRM data taken from a state-of-the-art Goddard multiscale modeling framework (GMMF) simulation.

The following section details the GMMF simulation output that is used as input to our radiative transfer calculations and the radiative transfer scheme used to perform these calculations, including new parametrizations of the single scattering properties of rain. Section 3 describes the radiative effect of rain at a range of scales, from global mean to instantaneous individual CRM profiles. Section 4 outlines the factors that determine the magnitude and direction of the radiative effect of rain. We conclude this article with a summary of the results and a brief discussion of the implications for LSAMs.

2. Methods

2.1. GMMF Simulation

To properly assess the global radiative effect of rain, simultaneous profiles of both precipitating and suspended hydrometeors are required, including both light and heavy precipitation, over both land and ocean. Unfortunately, no existing observations are able to fulfill all the criteria required. For example, the 17-year satellite-based Tropical Rainfall Measuring Mission radar provided vertical profiles of rainwater content (Iguchi et al., 2000) but not suspended hydrometeors. Products based on the CloudSat cloud profiling radar instrument include both suspended and precipitating hydrometeor profiles over ocean, but no retrievals of rain profiles exist over land (Lebsock & L'Ecuyer, 2011; L'Ecuyer & Stephens, 2002). In the absence of suitable observational data, we rely on detailed simulations. Global models and reanalyses can provide comprehensive global data sets, but lack the small-scale hydrometeor data required to accurately calculate the RRE. CRMs provide the high-resolution vertically resolved structure of both suspended and precipitating hydrometeors required for our radiative transfer calculations, but lack global coverage. In order to attain both global coverage and small-scale hydrometeor data, we use output from a multiscale modeling framework (also known as *super-parametrization*) simulation where a global atmospheric model is run with a CRM embedded within each gridbox. This framework provides a global ensemble of CRM data and has previously proved useful for analyzing the radiative effect of other processes that are not usually included in LSAMs, such as subgrid-scale cloud radiation interactions (Cole, Barker, Randall, et al., 2005) and three-dimensional effects (Cole, Barker, OŠHirok, et al., 2005).

For this study, we use data from a GMMF simulation that couples the Goddard Earth Observing System (GEOS; a global atmospheric model) with the Goddard Cumulus Ensemble Model (GCE; a CRM). Specifically, the GMMF simulation referred to as the L2014 experiment in Chern et al. (2016) was used. Of the four simulations analyzed in that study, the L2014 simulation had the most complete cloud microphysical scheme. The L2014 also generally had among the smallest errors compared to all the observations considered in that study, including TOA radiation, cloud fractions, and hydrometeor water paths. The simulation was run from 1 December 2006 to 31 December 2008, with weekly sea surface temperatures from the NOAA optimum interpolation

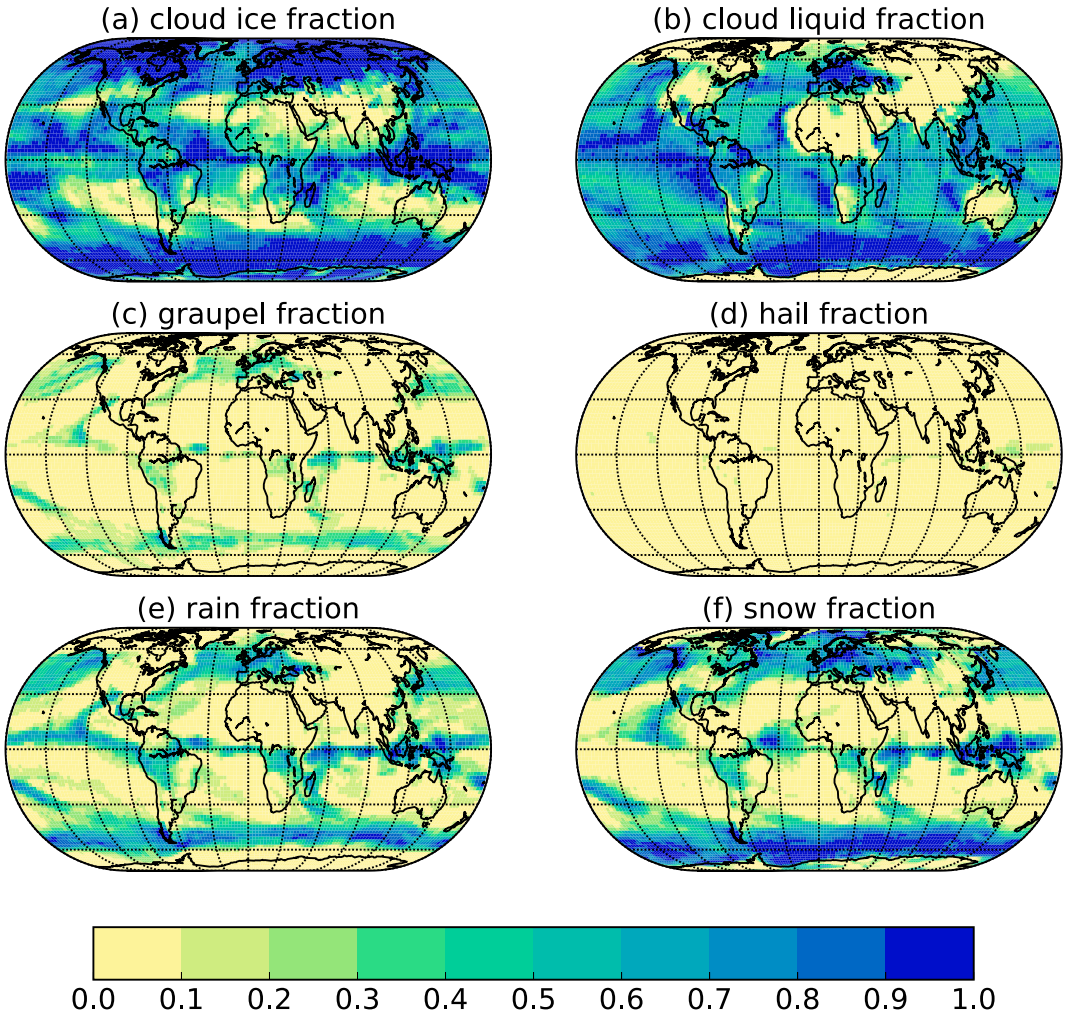

Figure 1. Distributions of mean fractions of the hydrometeor species in the Goddard multiscale modeling framework simulation for 1–7 January 2007 based on a layer mass mixing ratio threshold of 10^{-7} kg/kg.

data set (Reynolds et al., 2007) and initial conditions based on the ERA-Interim reanalysis (Dee et al., 2011). The GEOS model was run with a horizontal resolution of 2° latitude and 2.5° in longitude, and 48 layers in the vertical. The GCE CRM embedded within each GEOS grid box was run in two dimensions, with 32 columns each 4 km wide and 44 layers. We refer to the GCE columns as CRM profiles hereafter.

All hydrometeors are handled by the CRM, which uses a single moment bulk microphysics scheme (Lang et al., 2014; Tao et al., 2016). Six hydrometeor species are represented: cloud liquid, rain, cloud ice, snow, graupel, and hail. The hydrometeor species are treated as horizontally homogeneous within the CRM profiles (i.e., there is no fractional occurrence of the hydrometeors within the CRM profiles). Radiation calculations in the GMMF are also handled by the CRM and all six hydrometeor species are included in the radiation calculations (e.g., Tao et al., 2003). Further details of the GMMF setup for this simulation can be found in Chern et al. (2016).

Our analysis is based on hourly output from 2 weeks of GMMF simulated data, 1 week each in Boreal Winter (1–7 January 2007) and Boreal Summer (1–7 July 2007). This corresponds to more than 140 million CRM profiles. Figures 1, 2a, and 2b show the mean area fractions of the six hydrometeors species in these CRM profiles. A number of key features are found in these figures. First, all species generally have peak fractions in the tropics corresponding to the Intertropical Convergence Zone (ITCZ) and at ~50° north and south corresponding to midlatitude storm tracks, with minima in the subtropics corresponding to the subsidence zones. Second, the suspended hydrometers (i.e., cloud liquid and cloud ice) occur more frequently than the precipitating hydrometeors. Among precipitating hydrometeors, snow has the largest area fraction, while the rain fraction is similar to snow at low latitudes but smaller at high latitudes. The graupel fraction is generally less

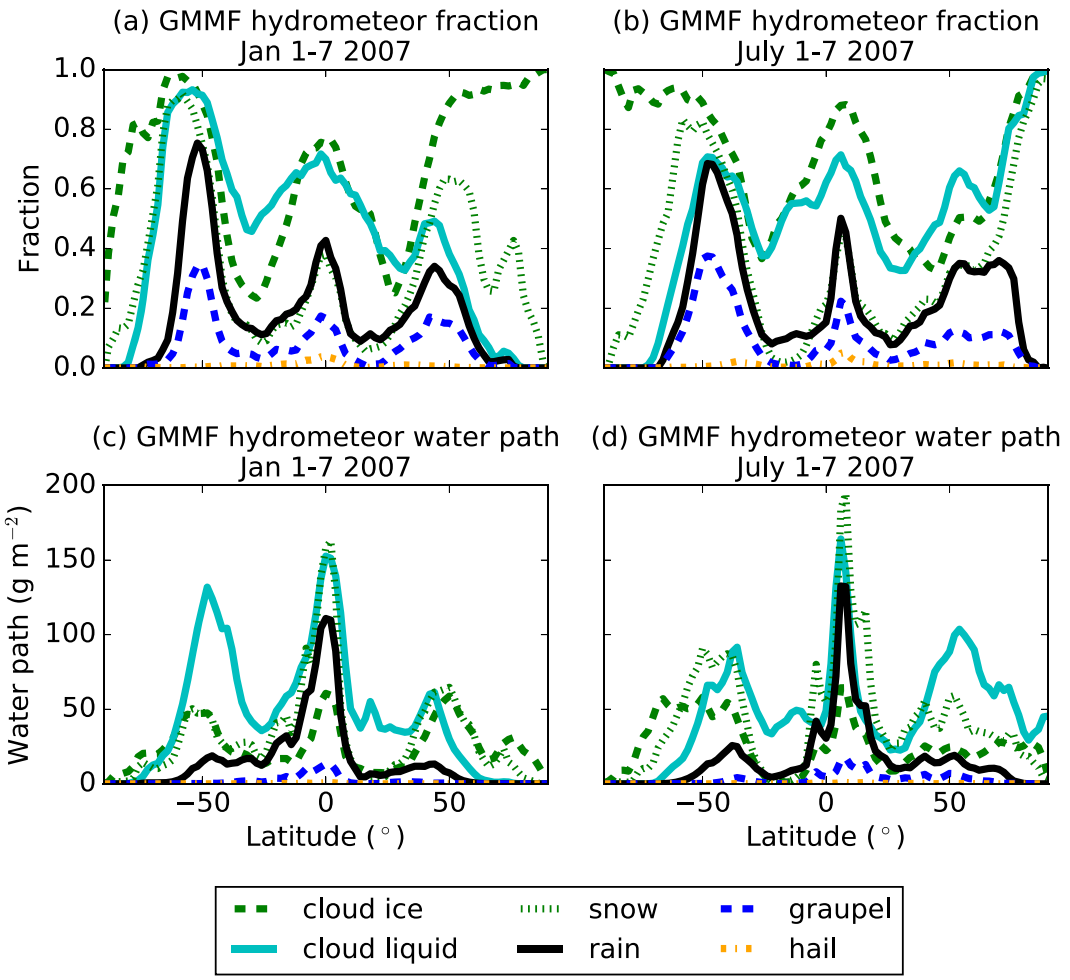

Figure 2. Zonal mean fractions (a,b) and water paths (c,d) of the six hydrometeor species in the GMMF simulation for (a,c) 1–7 January and (b,d) 1–7 July 2007 based on a layer mass mixing ratio threshold of 10^{-7} kg/kg. GMMF = Goddard multiscale modeling framework.

than half that of rain and the hail fraction is smaller still. Finally, comparison between Figures 2a and 2b shows the expected interseasonal differences. The ITCZ is located further north during the boreal summer, while ice fractions increase at the expense of liquid in high latitudes during the winter.

Figures 2c and 2d show the zonal mean water paths. Similarly to the fractions, all species have water path maxima in the ITCZ and midlatitude storm tracks and minima in the subsidence zones. The interseasonal differences in the water path values also follow a similar pattern to those for the hydrometeor fractions. However, water path values in the ITCZ are much larger than those in the midlatitude storm tracks, particularly for rain.

Clearly, the credibility of our estimates of the RRE strongly depend on the realism of this GMMF hydrometeor data. Chern et al. (2016) showed that ice water content in this simulation is within the observational uncertainty. The realism of the other hydrometeors in the GMMF is harder to assess due to the aforementioned lack of reliable global precipitating hydrometeor data sets. The GMMF is thought to underestimate the global mean rain water path, while overestimating surface precipitation in the tropics (Chern et al., 2016), which is a common problem for multiscale modeling framework simulations (Tao et al., 2009). Consequently, we might expect to underestimate the RRE globally, while overestimating it in the tropics. Nevertheless, for reasons of physical consistency, if the radiative effect of rain in a model is significant, then the radiative effect of rain should be included in that model, irrespective of whether it is representative of the true radiative effect of rain. Consequently, even if the GMMF derived RRE is imperfect, it remains useful as an example of the magnitude of the RRE in a LSAM.

2.2. Representation of Hydrometeors in the SOCRATES Radiative Transfer Scheme

GMMF atmospheric profiles are used as input to off-line radiative transfer calculations using the SOCRATES radiative transfer scheme (Edwards & Slingo, 1996). This is a flexible one-dimensional radiative transfer scheme that is employed in both numerical weather prediction (NWP) and climate models. Our calculations are based on the two-stream approximation and use the correlated-k method to treat gaseous absorption. We use 21 k-terms in the SW spread between six spectral bands between 200 nm and 10 μm. We use 47 k-terms in the LW spread between nine spectral bands between 3.3 μm and 1 cm. Mixing ratios for the six hydrometeor species and water vapor, pressure, temperature, and surface albedos are based on GMMF output. Mass mixing ratios of oxygen, carbon dioxide, methane, and dinitrogen oxide are set to horizontally and vertically constant values. The LW surface emissivity is set to one, globally. Hydrometeor mass mixing ratios below 1.0×10^{-7} kg/kg are set to zero. We calculate radiative fluxes independently for each CRM profile. Aerosols are not included.

Radiative transfer calculations through hydrometeor layers require knowledge of the single scattering properties for each spectral band and each hydrometeor species, specifically the mass extinction coefficient β, the single scattering albedo ω, and the asymmetry factor g . The current version of SOCRATES accounts for the radiative effects of cloud liquid, cloud ice, and snow, but not other species. The single scattering properties of cloud droplets are calculated from the cloud liquid mass mixing ratio and effective radius provided by the GMMF, using the parametrization described by Edwards and Slingo (1996). The cloud droplet effective radius in the GMMF varies from 8 to 14 μm, depending on temperature and surface type. Suspended cloud ice and precipitating snow are treated as a single ice category in our calculations, with single scattering properties calculated from the ice plus snow mass mixing ratios and temperature provided by the GMMF, using the parametrization described by Baran et al. (2013). This parametrization is based on an ensemble of ice crystal shapes ranging from simple pristine ice crystals to complex snow aggregates (Baran & Labonnote, 2007) and does not discriminate between ice and snow. Consequently, we are unable to calculate a snow radiative effect and for the rest of this paper, we use *ice* to refer to the combination of both suspended ice (i.e., cloud ice) and precipitating ice (i.e., snow).

Since parametrizations of the single scattering properties of rain, graupel, and hail are not included in SOCRATES, new parametrizations were derived for these species. We shall describe this parametrization process in detail for rain. Rain droplets can be reasonably approximated as spheres (e.g., Beard et al., 2010), and Mie theory is applied to calculate the single scattering properties. We assumed a water density of 1,000 kg/m^3 for rain and the refractive index was taken from Hale and Querry (1973) in the SW and Downing and Williams (1975) in the LW. To ensure that the new parametrization is consistent with the rain mass mixing ratios and temperatures predicted by the CRM, we take the range of mass mixing ratios predicted by the CRM (1.0×10^{-7} to 5.0 kg/kg) and divide this into 250 evenly spaced bins. For each bin, we randomly sample eight CRM points with mass mixing ratios within the bin limits. For each point, we use the rain mass mixing ratio and corresponding temperature sampled from the GMMF to generate a distribution of rain droplet sizes across 1,000 bins, following the same hydrometeor mass mixing ratio and temperature dependent Marshall and Palmer (1948) distribution as the CRM microphysics scheme. Mie calculations are performed on this distribution to derive the rain single scattering properties for each combination of rain mass mixing ratio and temperature, for wavelengths between 0.2 μm and 2 cm.

Once the Mie calculations are complete, we average in wavelength space to calculate mean single scattering properties for each point for each of the SOCRATES spectral bands. In the SW, this averaging uses weighting by the incident TOA irradiance for each wavelength. In the LW, the averaging uses weighting by the thermal source function. For each SOCRATES spectral band, this leaves us with 2,000 combinations (8 points per bin times 250 bins) of mass mixing ratio (q) and effective radius (r_e, calculated from the size distribution of rain droplets) corresponding to 2,000 values of β, ω, and g. A least squares method is then used to parametrize this data set using the simple equations proposed by Slingo and Schrecker (1982). Further details of these parametrizations are available in Appendix A.

Despite the irregular shape of graupel and hail, we also use Mie theory to calculate their optical properties. Tang et al. (2017) demonstrated this to be a reasonable approximation. The optical properties of graupel and hail are parametrized in a manner analogous to those for rain, with two major differences. First, the refractive

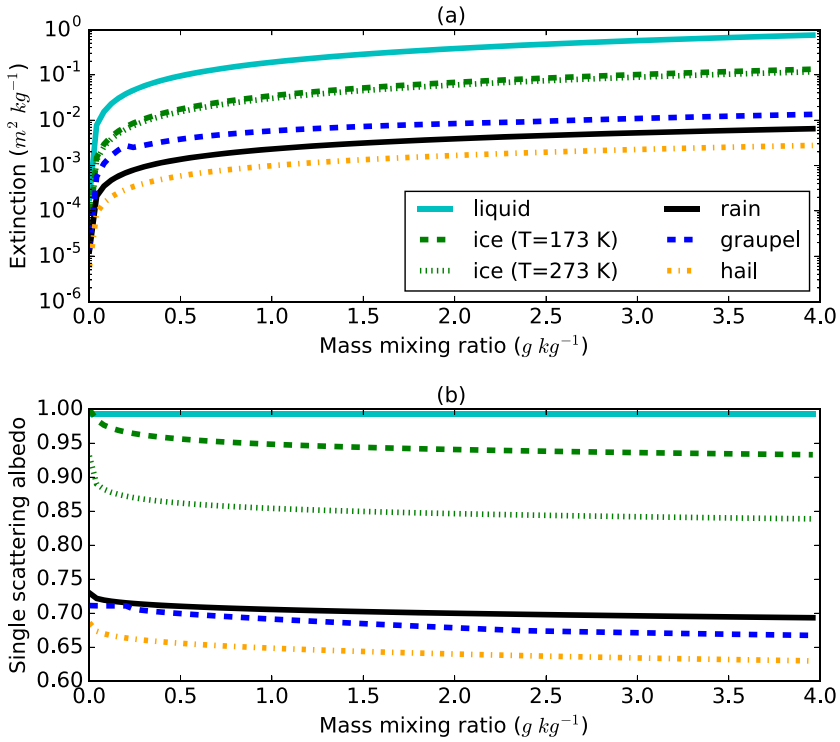

Figure 3. Parametrized single scattering properties for the different hydrometeor species as a function of their mass mixing ratio, for a shortwave spectral band at 1.19–2.38 μm wavelength used in Suite Of Community RAdiative Transfer codes based on Edwards and Slingo (1996).

index of ice is based on the review of Warren (1984), except for between 1.4 and 2.5 μm, where the imaginary part of the refractive index is based on the more recent and accurate measurements of Kou et al. (1993). Second, we assume ice densities of 300 kg/m^3 and 900 kg/m^3 for graupel and hail, respectively.

Figure 3 compares the newly parametrized extinction and single scattering albedo of rain, graupel, and hail to those of cloud liquid and ice at wavelengths between 1.19 and 2.38 μm, one of the SOCRATES spectral bands. Recall that the Marshall-Palmer size distributions used in the CRM depend on the mass of hydrometeor and temperature (section 2.1). For the purpose of this comparison, effective radii for these three species are calculated using these same CRM size distributions with a temperature of 273.15 K. This results in effective radii of 116–920 μm for rain, 300 μm–2.4 mm for hail, and 1.8–3.9 mm for graupel, for the mass mixing ratio range given in Figure 3, with larger effective radii for larger mass mixing ratios. For liquid, we use the same temperature of 273.15 K and assume the cloud is over land, resulting in a cloud droplet effective radius of 8 μm. For ice, the parametrization described in Baran et al. (2013) was designed to avoid the concept of effective radii and has a stronger temperature dependence. We therefore plot the ice single scattering properties at two temperatures, 173.15 and 273.15 K, which demonstrates the range of possible values from this parametrization.

As shown in Figure 3a, the extinction due to rain, graupel, and hail is at least an order of magnitude smaller than for the same mass of ice or liquid. Although the extinction for each hydrometeor species varies with wavelength, the relative magnitude of the extinction for each hydrometeor species in the other spectral bands is similar to that shown here. Additionally, Figure 3b shows that the parametrized single scattering albedo for rain, graupel, and hail is much smaller than that for liquid cloud and ice. This is because the single scattering albedo generally decreases as the particle size increases (e.g., Slingo & Schrecker, 1982), and rain, graupel, and hail particles are larger on average than cloud droplets, ice crystals, and snow aggregates. Again, the relative magnitude of the single scattering albedo for each hydrometeor species in the other spectral bands is similar to that shown in Figure 3a.

Table 1
Area Weighted Global Mean Radiative Effect of Rain, Graupel, Hail, and Cloud (All Hydrometeors) Derived From 2 Weeks (One Winter, One Summer) of Hourly Goddard Multiscale Modeling Framework Data

Radiative effect (W m^{-2})	All hydrometeors	Rain	Graupel	Hail
LW TOA	2.0×10^{1}	6.7×10^{-3}	5.9×10^{-3}	1.1×10^{-5}
SW TOA	-4.4×10^{1}	-3.4×10^{-2}	3.2×10^{-3}	-7.0×10^{-6}
Net TOA	-2.4×10^{1}	-2.7×10^{-2}	9.1×10^{-3}	3.9×10^{-6}
LW surface	2.5×10^{1}	1.6×10^{-1}	1.8×10^{-3}	1.6×10^{-5}
SW surface	-4.8×10^{1}	-1.0×10^{-1}	-1.3×10^{-2}	-7.7×10^{-5}
Net surface	-2.3×10^{1}	6.4×10^{-2}	-1.1×10^{-2}	-6.1×10^{-5}
LW in-atmosphere	-5.7×10^{0}	-1.6×10^{-1}	4.2×10^{-3}	-5.4×10^{-6}
SW in-atmosphere	4.0×10^{0}	6.6×10^{-2}	1.6×10^{-2}	7.0×10^{-5}
Net in-atmosphere	-1.7×10^{0}	-9.1×10^{-2}	2.0×10^{-2}	6.5×10^{-5}

Note. LW = longwave; SW = shortwave; TOA = top of atmosphere.

3. The Radiative Effect of Rain

To assess the radiative effect of rain, we examine the difference between two experiments. The first experiment, denoted as *all_hydro* is our control experiment, including all six hydrometeor species in our radiative transfer calculations. In the second experiment, denoted as *no_rain*, we exclude rain by setting its mixing ratio to zero in the radiation scheme for all grid points. For completeness, we also calculate graupel and hail radiative effects using additional *no_graupel* and *no_hail* experiments that exclude graupel and hail, respectively. Finally, to put these results in context, we perform a clear-sky experiment, excluding all suspended and precipitating hydrometeors, which is used to calculate the total hydrometeor radiative effect.

From these experiments, the radiative effect of each precipitating hydrometeor species is given by

$$RE = (I^{\downarrow}_{all} - I^{\uparrow}_{all}) - (I^{\downarrow}_{noj} - I^{\uparrow}_{noj}), \tag{1}$$

where $I^{\downarrow}$ and $I^{\uparrow}$ denote the downwelling and upwelling irradiance, respectively. The subscript *all* denotes irradiances from the all_hydro experiment, while *no j* denotes irradiances from the experiment that excludes the j-hydrometeor species, such as no_rain, no_graupel, or no_hail. Using rain as an example, the RRE can be calculated by

$$RRE = (I^{\downarrow}_{all} - I^{\uparrow}_{all}) - (I^{\downarrow}_{no\_rain} - I^{\uparrow}_{no\_rain}). \tag{2}$$

This definition is analogous to the commonly used cloud radiative effect (CRE), where clear sky is a *no_cloud* calculation. This definition is applied to both TOA and surface radiative effects, while the in-atmosphere radiative effect is calculated as the difference between the TOA and surface radiative effects and provides a measure of the vertically integrated change in absorption by the atmosphere and hence heating of the atmosphere. In practice, rain may cause both heating and cooling at different heights within the same atmospheric column. Consequently, the vertically integrated heating may have a smaller magnitude than the heating of individual layers within a column.

3.1. Global Mean RRE

Using equation (1), we derived the global, area-averaged mean radiative effects of rain, graupel, hail, and all hydrometeors (Table 1). The mean CRE (i.e., all hydrometeors) is included to provide context for the radiative effects of the precipitating hydrometeors. The RRE has the same signs as CRE in all SW and LW quantities listed in Table 1, but with much smaller magnitudes as expected from Figures 2 and 3. At the TOA and the surface, absorption and emission of LW radiation by rain increases the net downward LW irradiance, while reflection and absorption of SW radiation reduces the net downward SW irradiance. The opposing effects on LW and SW net irradiances lead to a smaller total net RRE, which has the same sign as the CRE at the TOA and in-atmosphere. At the surface, where the net CRE is negative, the net RRE is positive due to rain occurring closer to the surface than clouds, leading to relatively large LW warming of the surface. Since the RRE at the TOA and the surface is at least an order of magnitude smaller than the current observational irradiance uncertainty

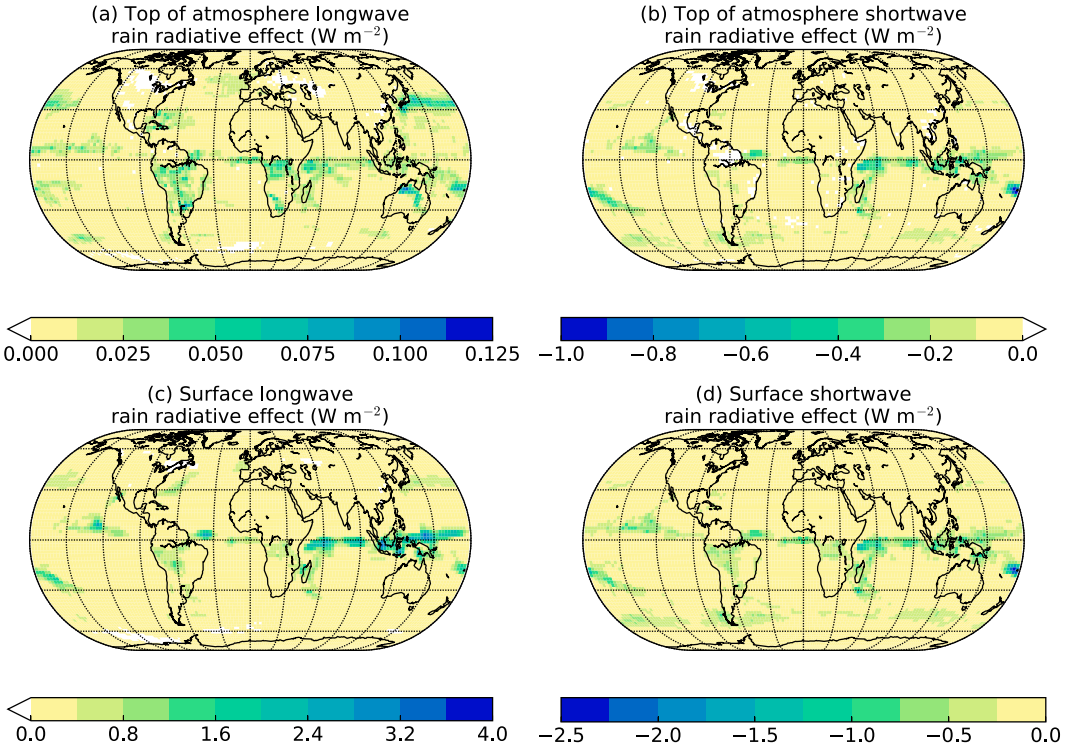

Figure 4. Mean radiative effect (W m^{-2}) of rain, based on the Goddard multiscale modeling framework simulations for 1–7 January 2007.

(e.g., Stephens et al., 2012), and the total net radiative effect is much smaller than CRE, we conclude that the contribution of rain to the *global mean* radiation budget is negligible.

Graupel and hail global mean radiative effects are much smaller than the RRE, which is not surprising considering that graupel and hail occur much less frequently than rain (as shown in Figure 2). Hail has the same sign SW and LW radiative effects as rain and cloud, but the graupel radiative effect has the opposite sign for the SW at the TOA and the LW in the atmosphere. The change of the sign in the SW is because graupel absorbs sunlight that would otherwise be reflected by liquid or ice clouds. The change of the sign in the LW is because graupel commonly occurs high enough that the TOA LW radiative effect is much larger than the surface LW radiative effect, much like ice clouds (e.g., Hong et al., 2016). As the graupel and hail radiative effects are much smaller than rain, we shall focus on rain in the rest of this article.

3.2. Spatial Distribution of the RRE

The distribution of RRE correlates strongly with the occurrence of rain. The largest LW RRE at the TOA occurs in the ITCZ and storm tracks (Figure 4a), where rain occurs most frequently (see Figures 1 and 2). This pattern is repeated in the LW RRE at the surface (Figure 4c) and in the SW (Figures 4b and 4d), but with different magnitudes. At the surface, the LW RRE is much larger than at the TOA, up to 4 W m^{-2} in the ITCZ where the rainwater paths are largest (Figure 2c). In the SW, the RRE at the surface is about twice as large as the RRE at the TOA, due to absorption of sunlight by rain. At both the TOA and the surface, the SW RRE is larger in the ITCZ than in the midlatitude storm tracks, again due to larger rainwater paths in the ITCZ. Similar patterns are also found in the RREs for 1–7 July 2007 (not shown), but with the ITCZ and associated RRE shifted slightly further north (cf. Figure 2), with increased SW RRE in the northern hemisphere and decreased SW RRE in the southern hemisphere due to the seasonal changes in TOA incoming SW irradiance.

3.3. RRE at the CRM Scale

While rain may not have a large impact on the global mean radiation budget, this does not mean that the RRE never reaches values that are sufficiently large and occur sufficiently often to systematically influence the evolution of a LSAM. To investigate the range of RRE, Figure 5 shows the normalized frequency distribution of LW and SW RRE at the TOA, surface, and in-atmosphere at the CRM column scale (i.e., a grid box of ~4 km). The distributions are based on 1.0 W m^{-2} bins and include only those points where rain occurs. In order to

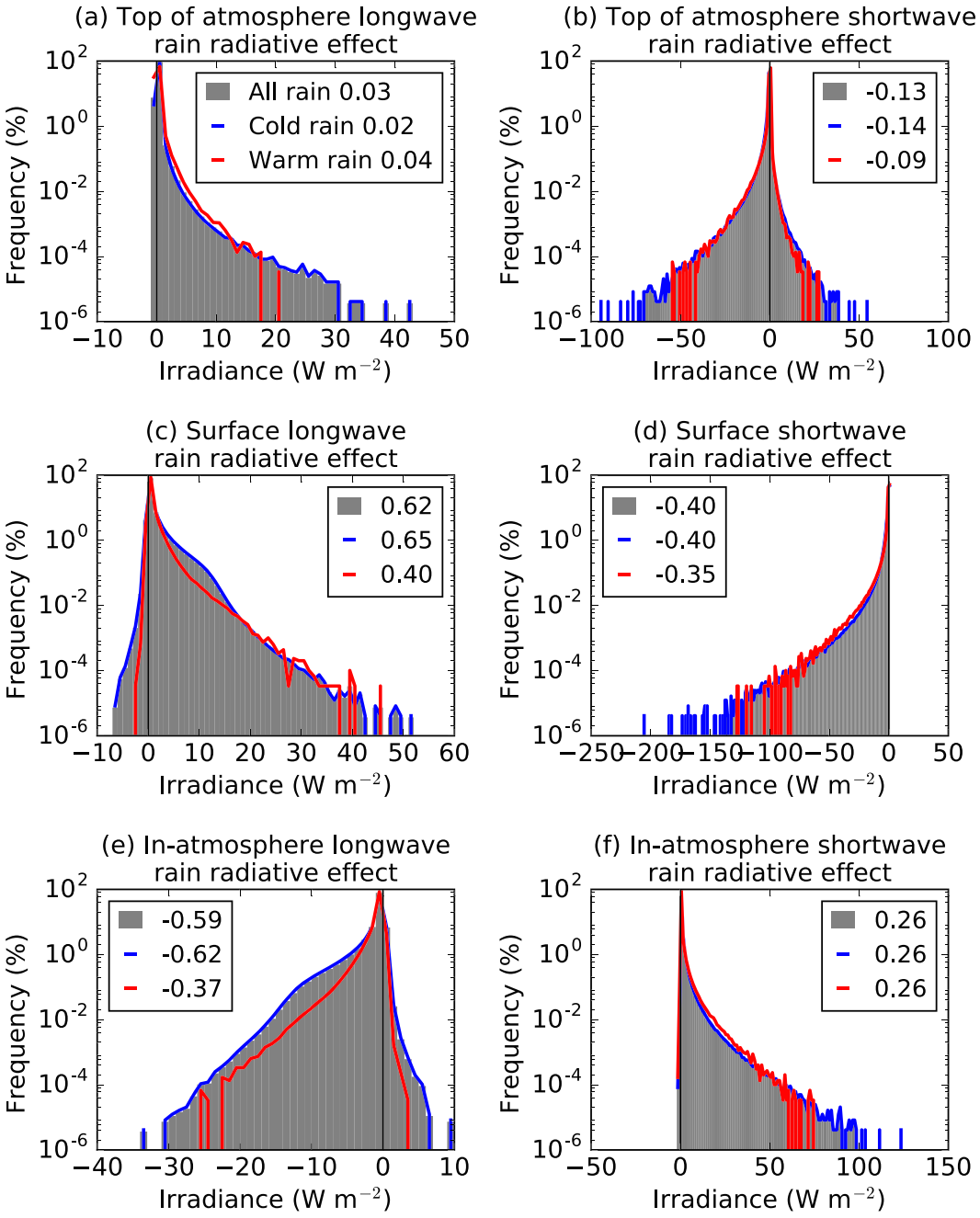

Figure 5. Frequency distributions of rain radiative effect for 1–7 January and 1–7 July 2007 combined at top of atmosphere (top row), surface (middle), and in-atmosphere (bottom) for longwave (left) and shortwave (right). Bin width is 1.0 W m^{-2}. The red line, blue line, and gray bars show the distributions for warm, cold, and all rain, respectively. Note that we only include grid boxes where rain is present in these distributions. The numbers in the legend show the means of the distributions.

highlight the full range of RRE, we use a log-scale for the frequency (*y* axis). For the SW, we include all daylight points, so that the spread in the distribution is partially due to variation in solar zenith angles.

The largest magnitude LW RRE values in Figure 5 are approximately 100 times larger than both the global mean values (see Table 1) and the mean RRE when rain occurs (see the numbers in the legends in Figure 5). We can see that LW RRE values at TOA, surface, and in-atmosphere can all be either positive or negative; the cancelation between positive and negative RREs partly explains the small global mean RREs. Recall that Savijärvi and Räisänen (1998) reported a LW surface RRE of 24 W m^{-2} for a cloud with base at 3 km and a surface rain

rate of 100 mm/hr. Figure 5c shows that LW RREs of this magnitude are possible but rare (occurring in approximately one in a hundred thousand rainy columns). Under similar conditions (i.e., cloud base height of at least 3,000 m and rain rate of at least 100 mm/hr) our calculations give a mean surface LW RRE of 14.8 W m^{-2}, which is considerably smaller than the value reported by Savijärvi and Räisänen (1998). This is to be expected as Savijärvi and Räisänen (1998) point out that their estimates are likely to be too large due to an unrealistically dry atmosphere below cloud base. Even more moderate LW surface RREs of 10 W m^{-2} or greater are infrequent, occurring in only 0.4% of the rainy CRM columns.

As mentioned earlier, the SW RRE distribution includes changes due to solar zenith angle; the largest RREs generally correspond to cases with small solar zenith angles, due to a larger amount of incoming solar radiation to be potentially absorbed or reflected. Similar to the LW, SW RRE values at TOA, surface, and in-atmosphere can also all be either positive or negative. However, positive surface SW RRE values are very rare (less than 0.01% of rainy daytime columns) and have very small magnitude (less than 0.5 W m^{-2}). Negative in-atmosphere SW RRE are also rare (less than 0.05% of rainy daytime columns) with small magnitude (less than 2.0 W m^{-2} in magnitude). Savijärvi et al. (1997) reported an in-atmosphere SW RRE of up to 65 W m^{-2} for an idealized heavily precipitating case with overhead sun. The distribution of RREs shown in Figure 5f shows that SW RREs of this magnitude are possible but rare (occurring in less than 0.001% of rainy columns). In our GMMF data set, most of the heavily precipitating cases have large amounts of cloud water, and thus reflect large amounts of sunlight above the rainy layers, which reduces the amount of SW radiation that interacts with rain, making large RREs very unlikely. Even at the surface, where the magnitude of the SW RRE is largest, only 0.8% of rainy daytime cases have a RRE with a magnitude as large as 10 W m^{-2}.

To investigate potential links between the RRE and rain formation processes, Figure 5 also shows separate distributions for warm and cold rain. Our method for separating warm and cold rain is similar to Mülmenstädt et al. (2015): when the rain-producing cloud contains ice phase hydrometeors, we assume that the rain is due to ice phase processes and denote this cold rain, otherwise warm rain is assumed. According to this separation, of the 19% of CRM columns that contain rain, 89% are cold rain and 11% are warm rain. Thus, the total RRE is dominated by cold rain and the mean RREs for all rain are much closer to those for cold rain than those for warm rain (see legends in Figure 5).

There are clear differences between the RRE distributions for warm rain and cold rain. Beginning with TOA LW irradiances, the cold rain mean RRE is slightly smaller than the warm rain mean RRE (see legend for Figure 5a). This is because ice cloud is more likely to be present above the rain in the cold rain cases, which absorbs and emits radiation at lower temperatures and thereby reduces the impact of the rain on the TOA LW irradiances. In contrast, at the surface and in-atmosphere, the cold rain LW RRE is approximately 50% larger than the warm rain RRE. This is because the mean rain water path of 86.0 g/m^2 for cold rain is larger than that of 36.5 g/m^2 for warm rain.

In the SW, the larger mean rain water path in cold rain columns also leads to a larger mean RRE than for warm rain columns, both at the TOA and the surface (Figures 5b and 5d). However, the mean SW in-atmosphere RRE has a similar magnitude for both cold rain and warm rain (Figure 5f) due to two opposing factors. Cold rain columns have larger absorption by rain than warm rain columns. However, the reduction in absorption by cloud below rain is also larger for cold rain columns than for warm rain columns. The larger increase in absorption by rain for cold rain columns is caused by the larger mean rain water path and droplet effective radius for cold rain columns. The larger decrease in absorption by cloud for cold rain columns is because the single scattering albedo of cloud ice is smaller than that of cloud liquid (Figure 3) and extinction by rain reduces the amount of radiation available to be absorbed by any cloud below. Consequently, there is a larger decrease in cloud absorption for cold rain where there is more likely to be ice cloud below the rain with a smaller single scattering albedo.

4. What Controls the RRE?

We have shown that for individual CRM columns, the RRE can take a broad range of values, both positive and negative. In this section we identify the processes that determine the direction and magnitude of the RRE. Detailed analysis of two example hydrometeor and irradiance profiles over northern Canada and the central equatorial Pacific Ocean with very different RREs is used to illustrate how these processes affect the RRE. Further analysis of all rainy columns shows that the results from the case studies can be generalized to other columns.

Table 2
Details of the Two Case Studies Used to Illustrate the Radiative Effects of Rain

Location	Pacific Ocean	Northern Canada
Latitude	8°N	64°N
Longitude	145°W	85°W
Date	6 Jan 2007	3 July 2007
Time (UTC)	01:00	15:00
Local solar time (approx.)	15:00	09:15
Surface rain rate (mm/hr)	3.9	0.2
SW insolation (W m^{-2})	751	895
TOA LW RRE (W m^{-2})	0.1	0.3
TOA SW RRE (W m^{-2})	−15.4	6.5
Surface LW RRE (W m^{-2})	7.8	−0.1
Surface SW RRE (W m^{-2})	−37.5	−1.8

Note. LW = longwave; SW = shortwave; TOA = top of atmosphere; RRE = rain radiative effect.

4.1. Case Studies

The two case studies consist of individual CRM profiles and represent different vertical cloud structures: almost all the rain occurs below cloud base in the Pacific case; whereas about half the rainy layers are above the warm cloud in the Canadian case. Ice clouds are physically thicker with larger mass mixing ratios in the Canadian case. Together, these cases demonstrate that the RRE is determined not only by the rain water path itself, but also the relative water path with respect to other species and the location of the rain layer. Details of these case studies are given in Table 2.

The Pacific Ocean case is an example of the rain layer occurring below a liquid cloud layer. This case consists of a CRM column located at the edge of a tropical cumulus congestus cloud (Figure 6a) and has the larger rain mass mixing ratios of the two cases. Rain occurs between 600 hPa (~5,000 m) and the surface, falling from a ~1,500 m thick layer consisting of liquid cloud (occupying a single model layer ~500 m thick) and graupel (two model layers, each ~500 m thick) that sits just below the top of the congestus cloud in the neighboring column. The cirrus cloud layer at ~80 hPa occupies only a single model layer and is independent of the cumulus congestus cloud.

In the LW, the downwelling radiation emitted by the rain reaches the surface unimpeded by cloud. Rain is warmer than the cloud above it and thus increases the downwelling irradiance to the surface. In contrast, the liquid cloud above the rain absorbs and emits LW radiation and impedes the upwelling radiation emitted by the rain. As a result, the net irradiance at the surface increases, but the change at TOA is rather small, as shown in Figure 6b. In the SW, by reflecting sunlight, rain increases the upwelling SW irradiance from the lowest rainy layer to the TOA (Figure 6c), leading to a negative RRE at TOA. Reflection and absorption of sunlight also leads to a reduction in the downwelling irradiance from the highest rain layer to the surface (Figure 6c), and thus a negative RRE at the surface. The RREs in the Pacific case are particularly large due to the large rain mass mixing ratios, which lead to larger extinction (Figure 3a) and small cloud water path, which means that large amounts of SW radiation reach the rain layer.

In the Canadian case, the rain layer extends above the warm cloud. This case is a CRM column located at the leading edge of a cold front (Figure 6d). The rain layer in this case is a little shallower than the Pacific Ocean case, with smaller rain mass mixing ratios and more complex cloud structure in the vertical. Snow and graupel fall from a convective anvil at 500–700 hPa, with the snow melting to form rain at ~625 hPa (~4,000 m), which falls through an optically thick warm cloud that extends from ~800 hPa (~1,500 m) to the surface. A temperature inversion, caused by the passage of the cold front, occurs between the surface and ~950 hPa.

In the LW, the rain causes an increase in the downwelling LW irradiance above the warm cloud top, but this is rapidly reduced below the warm cloud top, as emission by cloud dominates over that from rain. As the liquid mass mixing ratio decreases near the surface, the rain effect is no longer completely overshadowed by the cloud effect, though it remains small. The temperature inversion means that rain emits radiation at

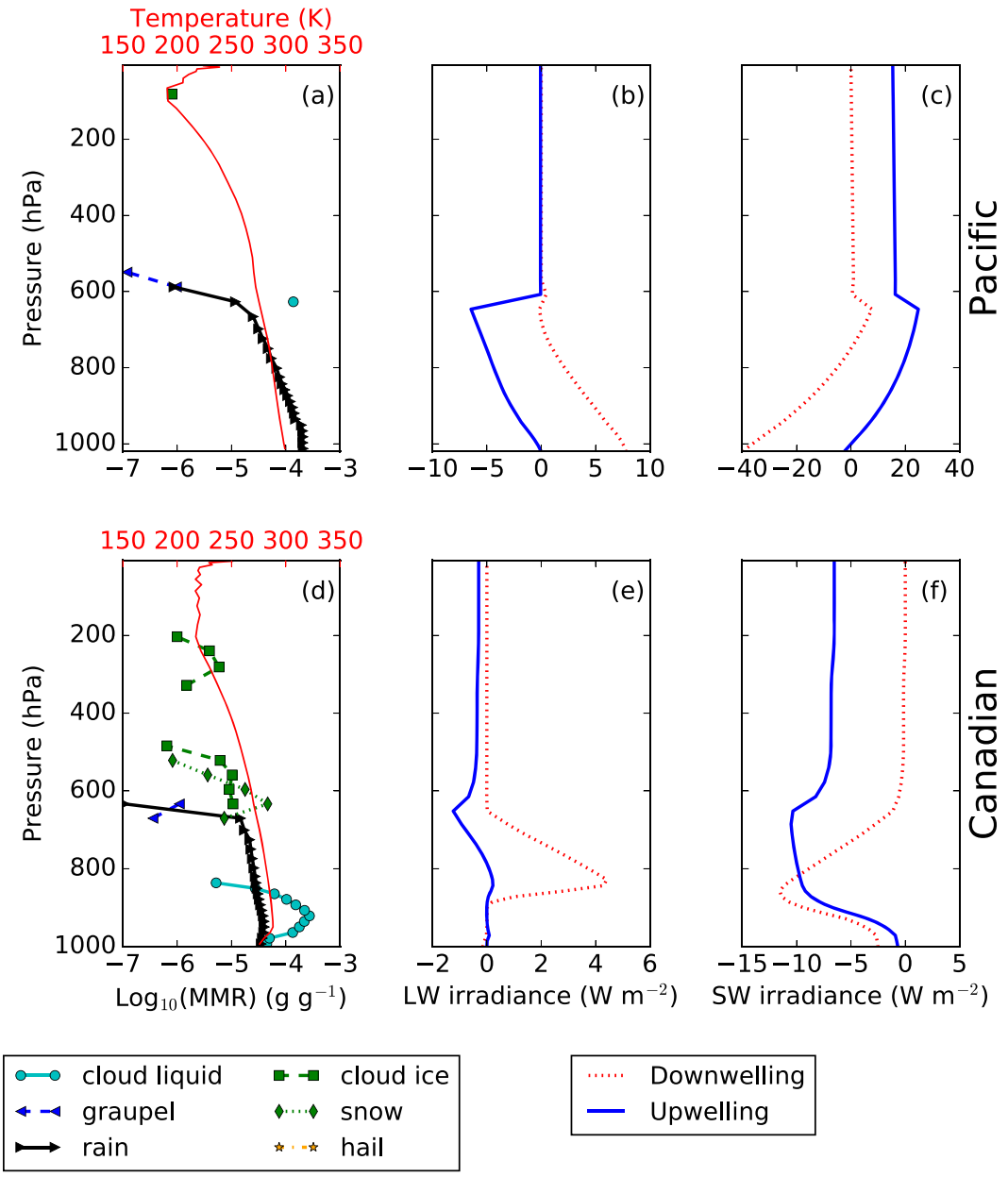

Figure 6. Examples of cloud resolving model columns with contrasting rain radiative effects. The top row shows the Pacific Ocean case and the bottom row shows the Northern Canada case. The left column shows MMR profiles for the six different hydrometeor species (black and gray) and the temperature profile (red). The middle column shows the corresponding all_hydro−no_rain LW profiles and the right column shows the corresponding all_hydro−no_rain SW profiles. MMR = mass mixing ratio.

colder temperatures than the cloud above, so that rain reduces the downwelling LW irradiance and the net effect at the surface is negative. Above the warm cloud, the reduction in upwelling irradiance due to rain is overshadowed by absorption and emission at colder temperatures by the ice cloud above. Consequently, the net RRE at the TOA is also very small. In the SW, the radiative effect of rain above cloud is analogous to the radiative effect of an absorbing aerosol layer above cloud (e.g., Chand et al., 2009; Wilcox, 2012). Since the absorbing rain layer is above the brighter cloud layer, sunlight is absorbed that would otherwise be reflected by clouds, resulting in a positive TOA SW RRE (see Table 2). For the downwelling SW irradiance, absorption and reflection by rain cause a reduction in irradiance, which decreases with altitude below the warm cloud top as

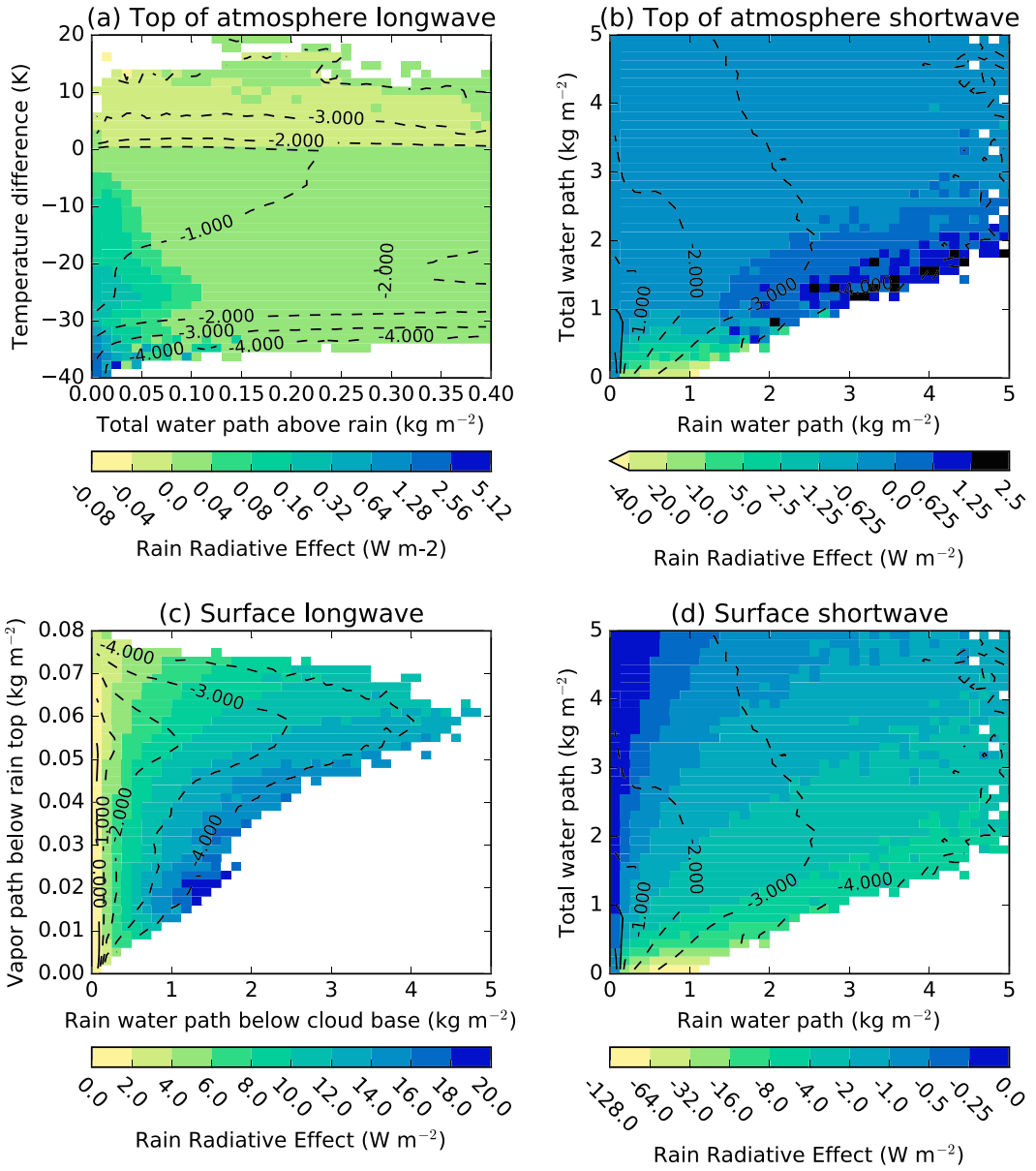

Figure 7. Rain radiative effect as a function of the state of the atmosphere, for all rainy cloud resolving model columns. Colors indicate the mean rain radiative effect in each X-Y bin (note the nonlinear color bars used). Contour lines indicate the percentage of the total number of rainy columns in each bin. Bins with fewer than 10 samples are not included. Panel (a) shows the mean top of atmosphere longwave RRE for the given values of the total water path above the uppermost rainy layer and the temperature difference between the uppermost rainy layer and the surface. Panel (b) shows the mean shortwave top of atmosphere RRE for given values of the rain water path and the total water path (which here includes vapor and all hydrometeors except rain), for lit points only. (c) shows the mean longwave surface RRE for given values of the rain water path below cloud base (here cloud includes liquid, ice, and snow) and the water vapor path below the uppermost rainy layer. Finally, (d) shows the mean shortwave surface RRE for given values of the rain water path and the total water path, for lit points only. RRE = rain radiative effect.

the radiation that is absorbed and reflected by the rain would have been reflected by the cloud anyway. As a result, the rain effect on the surface downwelling irradiance is quite small.

4.2. All Rainy Columns

The factors that have been identified as controlling the direction and magnitude of the RRE in these case studies can be generalized to all rainy profiles, as shown in Figure 7. This figure shows how the SW and LW

RREs at both the TOA and surface change as a function of the two main variables that we have identified as controlling the RRE. Note that these variables depend on the particular RRE in question.

Focusing first on the LW, Figure 7a shows that the total water path above the rain top plays a key role in limiting the LW TOA RRE. The RRE decreases rapidly as the total water path above rain top increases, because as explained for the case studies, any hydrometeors above the rain top impede the emission by rain. Figure 7a also shows that the LW TOA RRE is affected by the difference in temperature between the rain top and the surface. The magnitude of the LW TOA RRE increases as the magnitude of the difference increases. Generally, the rain top is cooler than the surface so the TOA LW RRE is positive as in both case studies. However, temperature inversions can lead to rain emitting at a higher temperature than the surface, leading to the negative TOA LW RRE seen in Figure 7a.

At the surface, Figure 7c shows that the LW RRE increases as the rain water path below cloud base increases, because the extinction depends on the rain mass mixing ratio, but (as explained in the Canadian case) any change in the downwelling irradiance due to rain above the cloud base will be overshadowed by emission from the cloud. The LW surface RRE decreases as the vapor water path below the rain top increases because absorption and emission by the vapor partly masks the emission by the rain. The rain water path below cloud base and vapor path below the rain top are positively correlated, so that the radiative effect of an increase in one tends to be offset by the effect of an increase in the other. In general, as temperature decreases with height, rain below cloud emits at higher temperatures than the cloud and increases the downwelling LW radiation, leading to a positive RRE. However, if a temperature inversion near the surface exists, the RRE can be negative, as seen in the Canadian case.

Moving to the SW, Figures 7b and 7d show both the surface and TOA RRE increase in magnitude with increasing rain water path (as extinction by rain depends on the rain mass mixing ratios) and decrease in magnitude as the total water path (excluding rain) increases (because less SW radiation reaches the rain layer). The rain and total water path values are positively correlated, so again in general the effect of an increase in one is offset by the effect of a increase in the other. At the TOA, the SW RRE is generally negative, with largest negative values when the total water path is small and the rain water path is large, as in the Pacific case. For total water path values larger than $\sim$1.5 kg/m^2, the mean RRE for the largest rain water path values is positive, as these cases tend to coincide with rain occurring above cloud base and absorbing radiation that would otherwise be reflected, as in the Canadian case.

At the surface, Figure 7d shows only negative values for the SW RRE. Analysis of the positive values shown in Figure 5d shows that positive SW RREs only occur when the solar zenith angle is very large, so that the albedo of both clouds and the surface is much larger for direct radiation than diffuse radiation. In some of these cases, including small amounts of rain can have little effect on the total downwelling SW irradiance, but lead to a large increase in the fraction that is diffuse. As the albedo for diffuse radiation of the cloud or surface below the rain is smaller than that for direct radiation, this can lead to an increase in the net downwelling surface SW irradiance.

5. Discussion

The aim of this study is to quantify the RRE. To our knowledge, this study is the first time that the RRE has been quantified globally. This represents a key step in determining whether rain needs to be included in the radiative transfer calculations applied in NWP and climate models.

From a global mean perspective, the RRE is very small, being less than 0.2 W m^{-2} for both SW and LW irradiances at the surface, TOA, and in-atmosphere. These mean values are a fraction of the accuracy with which we can measure global mean irradiances (e.g., Stephens et al., 2012) and consequently, from a global mean perspective, the RRE can be regarded as negligible. Averaging over a single week, at the GMMF gridbox scale, the RRE is largest for downwelling LW irradiance at the surface along the ITCZ, but remains less than 4 W m^{-2}. These largest RRE values are smaller than both the uncertainty in both the SW and LW global mean CREs (e.g., Stephens et al., 2012) and typical zonal mean TOA radiation errors seen in climate models (e.g., Dolinar et al., 2014). Moreover, the missing RRE can only explain a very small fraction of the persistent large (greater than 20 W m^{-2}) radiation errors seen in heavily precipitating regions in LSAMs.

At finer temporal and spatial scales, the RRE may be significant. At the finest scales available from the GMMF (i.e., the CRM column scale), the magnitude of the LW RRE can exceed 30 W m^{-2} at the surface, TOA, and in-atmosphere. For small solar zenith angles, the SW RRE can be even larger than this. Yet large RRE values are infrequent. For the LW surface RRE, less than 0.1% of the CRM columns have a RRE value larger than 10 W m^{-2}. Large RRE is more common for cold rain than warm rain events, primarily due to larger rain water path values for cold rain. The LW surface RRE exceeds 10 W m^{-2} for 0.47% of CRM columns identified as cold rain and 0.13% of those identified as warm rain. The RRE can be either positive or negative and the magnitude and direction depend on the vertical location with respect to any other hydrometeors, the properties of the surface, and in the LW the emission temperature of the rain and any other hydrometeors.

The calculations presented in this study were based on the assumption that the rain is in thermal equilibrium with the ambient air. In reality, evaporative cooling and falling from higher cooler altitudes may result in rain droplets that are cooler than the ambient air. Based on theoretical calculations and assuming a constant lapse rate, Best (1952) showed that evaporative cooling has a larger effect, except in the case of very large rain droplets. He found that rain droplets are up to 13 K cooler than the ambient temperature for a relative humidity of 40% and an ambient temperature of 314 K. This corresponds to a 15% decrease in the LW irradiance emitted by rain. However, for larger humidities, which generally coincide with rain, the temperature difference is much smaller, being less than 1 K at 95% relative humidity, which corresponds to a decrease in the LW irradiance emitted by rain of less than 1%.

Judging whether the exclusion of the RRE may negatively impact the evolution of a LSAM requires comparison of simulations where the RRE is and is not included interactively in that LSAM. However, previous studies have shown that LSAM simulations are rather insensitive to radiative errors of a much larger magnitude that do not persist in space or time (e.g., Barker et al., 2008; Bozzo et al., 2014; Hill et al., 2011). Moreover, given the transient nature of the RRE it seems highly unlikely to have a systematic effect on current LSAMs. Even when it is large the RRE is likely to be dwarfed by latent heating; for approximately 88% of CRM columns with a net downwelling surface LW RRE of at least 1.0 W m^{-2}, the surface latent heating is at least 10 times larger.

While the RRE is generally small, this study showed that at small scales the RREs can be quite large. Thus, it seems likely that at finer resolutions, the impact of the RRE on the realism of the simulation will increase. At high resolution, orographic enhancement of precipitation could lead to longer lasting large RREs at a fixed location. On this basis, the RRE is most likely to be significant for regional NWP models. Moreover, while this study indicates that excluding rain from LSAM radiative transfer calculations is unlikely to lead to large errors in models, it does still lead to errors and there is no reason not to include rain in LSAM radiative transfer calculations if the model already carries the required variables.

Appendix A : Rain, Graupel, and Hail Single Scattering Properties Parametrizations

Extinction (β), single scattering albedo (ω), and asymmetry (g) for rain, graupel, and hail are calculated using Mie theory as described in section 2.2. A least squares method is then used to parametrize this data set using the following simple equations proposed by Slingo and Schrecker (1982).

$$\beta = q \cdot (A + \frac{B}{r_e}), \tag{A1}$$

$$1 - \omega = C + D \cdot r_e, \tag{A2}$$

$$g = E + F \cdot r_e, \tag{A3}$$

where A, B, C, D, E, F are coefficients determined by performing the least square fitting with values given in the following tables. Tables A1, A2, and A3 show the values for the coefficients used in the parametrization of the single scattering properties of rain, graupel, and hail, respectively, for each of the six SW and nine LW bands.

Table A1
Parameters Derived for the Parametrization of the Single Scattering Properties of Rain

Wavelength (m)	A	B	C	D	E	F
Shortwave bands						
2.00×10^{-7}–3.20×10^{-7}	-9.9833×10^{-4}	1.5035×10^{-3}	3.1562×10^{-5}	2.0421×10^{0}	8.7270×10^{-1}	4.2819×10^{-1}
3.20×10^{-7}–6.90×10^{-7}	-1.4670×10^{-3}	1.5052×10^{-3}	6.6121×10^{-7}	1.2662×10^{-1}	8.8226×10^{-1}	1.3567×10^{-1}
3.20×10^{-7}–6.90×10^{-7}	-1.4670×10^{-3}	1.5052×10^{-3}	6.6121×10^{-7}	1.2662×10^{-1}	8.8226×10^{-1}	1.3567×10^{-1}
6.90×10^{-7}–1.19×10^{-6}	-2.3649×10^{-3}	1.5083×10^{-3}	1.9200×10^{-3}	1.2149×10^{1}	8.8564×10^{-1}	1.9942×10^{0}
1.19×10^{-6}–2.38×10^{-6}	-3.5276×10^{-3}	1.5124×10^{-3}	2.6483×10^{-1}	4.5330×10^{1}	9.2606×10^{-1}	9.8247×10^{0}
2.38×10^{-6}–1.00×10^{-5}	-6.8263×10^{-3}	1.5238×10^{-3}	4.6536×10^{-1}	3.7050×10^{-1}	9.7142×10^{-1}	1.0231×10^{-1}
Longwave bands						
3.34×10^{-6}–6.67×10^{-6}	-7.1358×10^{-3}	1.5248×10^{-3}	4.6489×10^{-1}	1.4904×10^{-1}	9.7039×10^{-1}	5.3054×10^{-2}
6.67×10^{-6}–7.52×10^{-6}	-9.4553×10^{-3}	1.5329×10^{-3}	4.6797×10^{-1}	-2.5385×10^{-1}	9.7361×10^{-1}	1.8214×10^{-2}
7.52×10^{-6}–8.33×10^{-6}	-1.0169×10^{-2}	1.5354×10^{-3}	4.6977×10^{-1}	-3.4776×10^{-1}	9.7568×10^{-1}	3.6619×10^{-2}
8.33×10^{-6}–1.25×10^{-5}	-1.0732×10^{-2}	1.5383×10^{-3}	4.7445×10^{-1}	-6.7541×10^{-1}	9.8106×10^{-1}	8.0455×10^{-2}
8.93×10^{-6}–1.01×10^{-5}	-1.1270×10^{-2}	1.5394×10^{-3}	4.7472×10^{-1}	-5.8781×10^{-1}	9.8107×10^{-1}	7.2116×10^{-2}
1.25×10^{-5}–1.82×10^{-5}	-1.3333×10^{-2}	1.5479×10^{-3}	4.5170×10^{-1}	-6.6916×10^{-1}	9.5177×10^{-1}	1.0014×10^{-2}
1.33×10^{-5}–1.69×10^{-5}	-1.3676×10^{-2}	1.5489×10^{-3}	4.4820×10^{-1}	-6.2890×10^{-1}	9.4747×10^{-1}	-1.8311×10^{-2}
1.82×10^{-5}–2.50×10^{-5}	-1.8573×10^{-2}	1.5656×10^{-3}	4.4060×10^{-1}	-1.1709×10^{0}	9.3037×10^{-1}	-4.1360×10^{-2}
2.50×10^{-5}–1.00×10^{-2}	-3.9201×10^{-2}	1.6537×10^{-3}	4.3890×10^{-1}	-6.5461×10^{0}	8.8105×10^{-1}	3.6852×10^{0}

Table A2
Parameters Derived for the Parametrization of the Single Scattering Properties of Graupel

Wavelength (m)	A	B	C	D	E	F
Shortwave bands						
2.00×10^{-7}–3.20×10^{-7}	-3.1038×10^{-3}	5.0115×10^{-3}	1.4616×10^{-6}	4.2090×10^{-1}	8.7621×10^{-1}	1.2914×10^{-1}
3.20×10^{-7}–6.90×10^{-7}	-4.7369×10^{-3}	5.0173×10^{-3}	3.8750×10^{-7}	9.4962×10^{-2}	8.8956×10^{-1}	1.2846×10^{-1}
3.20×10^{-7}–6.90×10^{-7}	-4.7369×10^{-3}	5.0173×10^{-3}	3.8750×10^{-7}	9.4962×10^{-2}	8.8956×10^{-1}	1.2846×10^{-1}
6.90×10^{-7}–1.19×10^{-6}	-7.4355×10^{-3}	5.0273×10^{-3}	6.1986×10^{-4}	7.4361×10^{0}	8.9428×10^{-1}	1.2573×10^{0}
1.19×10^{-6}–2.38×10^{-6}	-1.1152×10^{-2}	5.0407×10^{-3}	2.7466×10^{-1}	3.9109×10^{1}	9.3372×10^{-1}	8.0019×10^{0}
2.38×10^{-6}–1.00×10^{-5}	-2.0956×10^{-2}	5.0766×10^{-3}	4.6132×10^{-1}	1.1681×10^{0}	9.6803×10^{-1}	2.1389×10^{-1}
Longwave bands						
3.34×10^{-6}–6.67×10^{-6}	-2.2118×10^{-2}	5.0806×10^{-3}	4.6377×10^{-1}	-1.6486×10^{-3}	9.6825×10^{-1}	-7.6178×10^{-3}
6.67×10^{-6}–7.52×10^{-6}	-2.9064×10^{-2}	5.1061×10^{-3}	4.6716×10^{-1}	-2.5538×10^{-1}	9.7254×10^{-1}	1.0740×10^{-2}
7.52×10^{-6}–8.33×10^{-6}	-3.1406×10^{-2}	5.1146×10^{-3}	4.6806×10^{-1}	-3.3497×10^{-1}	9.7344×10^{-1}	2.5193×10^{-2}
8.33×10^{-6}–1.25×10^{-5}	-3.3325×10^{-2}	5.1243×10^{-3}	4.6418×10^{-1}	-4.9849×10^{-1}	9.6846×10^{-1}	3.4249×10^{-2}
8.93×10^{-6}–1.01×10^{-5}	-3.4940×10^{-2}	5.1277×10^{-3}	4.7456×10^{-1}	-5.8789×10^{-1}	9.8077×10^{-1}	7.1164×10^{-2}
1.25×10^{-5}–1.82×10^{-5}	-4.6831×10^{-2}	5.1717×10^{-3}	4.4659×10^{-1}	-7.2908×10^{-1}	9.4073×10^{-1}	-4.4234×10^{-2}
1.33×10^{-5}–1.69×10^{-5}	-4.7467×10^{-2}	5.1738×10^{-3}	4.4677×10^{-1}	-7.5554×10^{-1}	9.3977×10^{-1}	-4.8595×10^{-2}
1.82×10^{-5} – 2.50×10^{-5}	-6.1003×10^{-2}	5.2223×10^{-3}	4.5790×10^{-1}	$-1.134-\times10^{0}$	9.5445×10^{-1}	2.4309×10^{-1}
2.50×10^{-5}–1.00×10^{-2}	1.6860×10^{-1}	5.0053×10^{-3}	-8.1138×10^{0}	7.1646×10^{2}	-1.6628×10^{-2}	9.5776×10^{1}

Table A3
Parameters Derived for the Parametrization of the Single Scattering Properties of Hail

Wavelength (m)	A	B	C	D	E	F
Shortwave bands						
$2.00 \times 10^{-7} - 3.20 \times 10^{-7}$	-4.3479×10^{-4}	1.6689×10^{-3}	-7.0683×10^{-6}	4.2411×10^{-1}	8.7626×10^{-1}	1.0713×10^{-1}
$3.20 \times 10^{-7} - 6.90 \times 10^{-7}$	-7.4316×10^{-4}	1.6703×10^{-3}	-1.4956×10^{-6}	9.5675×10^{-2}	8.8971×10^{-1}	7.1167×10^{-2}
$3.20 \times 10^{-7} - 6.90 \times 10^{-7}$	-7.4316×10^{-4}	1.6703×10^{-3}	-1.4956×10^{-6}	9.5675×10^{-2}	8.8971×10^{-1}	7.1167×10^{-2}
$6.90 \times 10^{-7} - 1.19 \times 10^{-6}$	-1.1712×10^{-3}	1.6724×10^{-3}	7.8949×10^{-4}	7.3683×10^{0}	8.9447×10^{-1}	1.1832×10^{0}
$1.19 \times 10^{-6} - 2.38 \times 10^{-6}$	-1.4505×10^{-3}	1.6744×10^{-3}	3.0588×10^{-1}	2.6963×10^{1}	9.3851×10^{-1}	6.1403×10^{0}
$2.38 \times 10^{-6} - 1.00 \times 10^{-5}$	-2.7420×10^{-3}	1.6813×10^{-3}	4.6355×10^{-1}	3.0059×10^{-1}	9.6853×10^{-1}	1.9572×10^{-2}
Longwave bands						
$3.34 \times 10^{-6} - 6.67 \times 10^{-6}$	-2.8780×10^{-3}	1.6820×10^{-3}	4.6356×10^{-1}	7.7907×10^{-2}	9.6831×10^{-1}	-2.8267×10^{-2}
$6.67 \times 10^{-6} - 7.52 \times 10^{-6}$	-3.7901×10^{-3}	1.6869×10^{-3}	4.6652×10^{-1}	-7.5130×10^{-3}	9.7261×10^{-1}	-1.5754×10^{-2}
$7.52 \times 10^{-6} - 8.33 \times 10^{-6}$	-4.0923×10^{-3}	1.6886×10^{-3}	4.6731×10^{-1}	-4.3151×10^{-2}	9.7353×10^{-1}	-1.0611×10^{-2}
$8.33 \times 10^{-6} - 1.25 \times 10^{-5}$	-4.5065×10^{-3}	1.6912×10^{-3}	4.6316×10^{-1}	-1.0280×10^{-1}	9.6859×10^{-1}	-1.4137×10^{-2}
$8.93 \times 10^{-6} - 1.01 \times 10^{-5}$	-4.5538×10^{-3}	1.6911×10^{-3}	4.7348×10^{-1}	-1.6872×10^{-1}	9.8092×10^{-1}	1.3592×10^{-2}
$1.25 \times 10^{-5} - 1.82 \times 10^{-5}$	-6.1634×10^{-3}	1.6998×10^{-3}	4.4522×10^{-1}	-1.9536×10^{-1}	9.4084×10^{-1}	-8.7242×10^{-2}
$1.33 \times 10^{-5} - 1.69 \times 10^{-5}$	-6.2296×10^{-3}	1.7001×10^{-3}	4.4537×10^{-1}	-2.1024×10^{-1}	9.3987×10^{-1}	-8.9204×10^{-2}
$1.82 \times 10^{-5} - 2.50 \times 10^{-5}$	-7.9212×10^{-3}	1.7091×10^{-3}	4.5621×10^{-1}	-4.7367×10^{-1}	9.5506×10^{-1}	2.3164×10^{-3}
$2.50 \times 10^{-5} - 1.00 \times 10^{-2}$	1.0351×10^{-1}	1.5477×10^{-3}	-1.0529×10^{1}	1.6562×10^{3}	-1.1768×10^{-1}	1.3509×10^{2}

Acknowledgments
The research leading to this publication has received funding from the European Union 7th Framework Programme (FP7/2007-2013) under grant agreement 603502 (EU project DACCIWA: Dynamics-Aerosol -Chemistry-Cloud Interactions in West Africa). The authors would like to thank Adrian Hill for providing data and assistance for some precursor calculations of the rain radiative effect. The GMMF model outputs used in this study are available through NASA Cloud Library Data Portal (https://portal.nccs.nasa.gov/cloudlibrary/) upon request from Jiun-dar.chern-1@nasa.gov. The SOCRATES radiative transfer code including the modifications required to both derive single scattering properties of rain, graupel, and hail and to calculate their broadband radiative effects is available from the Met Office Science Repository Service (https://code.metoffice.gov.uk/trac/socrates/browser#main/branches/dev/peterhill/r58_hydrometeor_rad_effects). Results from the calculations are freely available from the University of Reading Research Data Archive at http://researchdata.reading.ac.uk/id/eprint/174.

References

Baran, A. J., Field, P., Furtado, K., Manners, J., & Smith, A. (2013). A new high- and low-frequency scattering parameterization for cirrus and its impact on a high-resolution numerical weather prediction model. *AIP Conference Proceedings*, *1531*, 716–719.

Baran, A. J., & Labonnote, L.-C. (2007). A self-consistent scattering model for cirrus. I: The solar region. *Quarterly Journal of the Royal Meteorological Society*, *133*(629), 1899–1912.

Barker, H. W., Cole, J. N. S., Morcrette, J.-J., Pincus, R., R"ais"anen, P., von Salzen, K., & Vaillancourt, P. A. (2008). The Monte Carlo Independent Column Approximation: An assessment using several global atmospheric models. *Quarterly Journal of the Royal Meteorological Society*, *134*, 1463–1478.

Beard, K. V., Bringi, V., & Thurai, M. (2010). A new understanding of raindrop shape. *Atmospheric Research*, *97*(4), 396–415.

Best, A. C. (1952). The evaporation of raindrops. *Quarterly Journal of the Royal Meteorological Society*, *78*(336), 200–225.

Bozzo, A., Pincus, R., Sandu, I., & Morcrette, J.-J. (2014). Impact of a spectral sampling technique for radiation on ECMWF weather forecasts. *Journal of Advances in Modeling Earth Systems*, *6*, 1288–1300.

Calisto, M., Folini, D., Wild, M., & Bengtsson, L. (2014). Cloud radiative forcing intercomparison between fully coupled CMIP5 models and CERES satellite data. *Annales Geophysicae*, *32*(7), 793–807.

Chand, D., Wood, R., Anderson, T. L., Satheesh, S. K., & Charlson, R. J. (2009). Satellite-derived direct radiative effect of aerosols dependent on cloud cover. *Nature Geoscience*, *2*(3), 181–184.

Chen, Y.-W., Seiki, T., Kodama, C., Satoh, M., & Noda, A. T. (2018). Impact of precipitating ice hydrometeors on longwave radiative effect estimated by a global cloud-system resolving model. *Journal of Advances in Modeling Earth Systems*, *10*(2), 284–296.

Chern, J.-D., Tao, W.-K., Lang, S. E., Matsui, T., Li, J.-L. F., Mohr, K. I., et al. (2016). Performance of the Goddard multiscale modeling framework with Goddard ice microphysical schemes. *Journal of Advances in Modeling Earth Systems*, *8*, 66–95.

Cole, J. N. S., Barker, H. W., O'Hirok, W., Clothiaux, E. E., Khairoutdinov, M. F., & Randall, D. A. (2005). Atmospheric radiative transfer through global arrays of 2D clouds. *Geophysical Research Letters*, *32*, L19817. https://doi.org/10.1029/2005GL023329

Cole, J. N. S., Barker, H. W., Randall, D. A., Khairoutdinov, M. F., & Clothiaux, E. E. (2005). Global consequences of interactions between clouds and radiation at scales unresolved by global climate models. *Geophysical Research Letters*, *32*, L06703. https://doi.org/10.1029/2004GL020945

Dee, D. P., Uppala, S. M., Simmons, A. J., Berrisford, P., Poli, P., Kobayashi, S., et al. (2011). The ERA-Interim reanalysis: Configuration and performance of the data assimilation system. *Quarterly Journal of the Royal Meteorological Society*, *137*(656), 553–597.

Dolinar, E. K., Dong, X., Xi, B., Jiang, J. H., & Su, H. (2014). Evaluation of CMIP5 simulated clouds and TOA radiation budgets using NASA satellite observations. *Climate Dynamics*, *44*(7-8), 2229–2247.

Downing, H. D., & Williams, D. (1975). Optical constants of water in the infrared. *Journal of Geophysical Research*, *80*(12), 1656–1661.

Edwards, J. M., & Slingo, A. (1996). Studies with a flexible new radiation code. 1: Choosing a configuration for a large-scale model. *Quarterly Journal of the Royal Meteorological Society*, *122*, 690–719.

Fu, Q., Krueger, S. K., & Liou, K. N. (1995). Interactions of radiation and convection in simulated tropical cloud clusters. *Journal of the Atmospheric Sciences*, *52*(9), 1310–1328.

Hale, G. M., & Querry, M. R. (1973). Optical constants of water in the 200-nm to 200-μm wavelength region. *Applied Optics*, *12*(3), 555–563.

Hill, P. G., Manners, J., & Petch, J. C. (2011). Reducing noise associated with the Monte Carlo Independent Column Approximation for weather forecasting models. *Quarterly Journal of the Royal Meteorological Society*, *137*(654), 219–228.

Hong, Y., Liu, G., & Li, J.-L. F. (2016). Assessing the radiative effects of global ice clouds based on CloudSat and CALIPSO measurements. *Journal of Climate*, *29*(21), 7651–7674.

Iguchi, T., Kozu, T., Meneghini, R., Awaka, J., & Okamoto, K. (2000). Rain-profiling algorithm for the TRMM precipitation radar. *Journal of Applied Meteorology*, *39*(12), 2038–2052.

Jiang, H., & Cotton, W. R. (2000). Large eddy simulation of shallow cumulus convection during BOMEX: Sensitivity to microphysics and radiation. *Journal of the Atmospheric Sciences*, *57*(4), 582–594.

Kou, L., Labrie, D., & Chylek, P. (1993). Refractive indices of water and ice in the 0.65- to 25-μm spectral range. *Applied Optics*, *32*(19), 3531–3540.

L'Ecuyer, T. S., & Stephens, G. L. (2002). An estimation-based precipitation retrieval algorithm for attenuating radars. *Journal of Applied Meteorology*, *41*(3), 272–285.

Lang, S. E., Tao, W.-K., Chern, J.-D., Wu, D., & Li, X. (2014). Benefits of a fourth ice class in the simulated radar reflectivities of convective systems using a bulk microphysics scheme. *Journal of the Atmospheric Sciences*, *71*(10), 3583–3612.

Lebsock, M. D., & L'Ecuyer, T. S. (2011). The retrieval of warm rain from CloudSat. *Journal of Geophysical Research*, *116*, D20209. https://doi.org/10.1029/2011JD016076

Li, J.-L. F., Forbes, R. M., Waliser, D. E., Stephens, G., & Lee, S. (2014). Characterizing the radiative impacts of precipitating snow in the ECMWF integrated forecast system global model. *Journal of Geophysical Research: Atmospheres*, *119*, 9626–9637. https://doi.org/10.1002/2014JD021450

Li, J.-L. F., Lee, W.-L., Waliser, D. E., David Neelin, J., Stachnik, J. P., & Lee, T. (2014). Cloud-precipitation-radiation-dynamics interaction in global climate models: A snow and radiation interaction sensitivity experiment. *Journal of Geophysical Research: Atmospheres*, *119*, 3809–3824. https://doi.org/10.1002/2013JD021038

Li, J.-L. F., Lee, W.-L., Waliser, D., Wang, Y.-H., Yu, J.-Y., Jiang, X., et al. (2016). Considering the radiative effects of snow on tropical Pacific Ocean radiative heating profiles in contemporary GCMs using A-Train observations. *Journal of Geophysical Research: Atmospheres*, *121*, 1621–1636. https://doi.org/10.1002/2015JD023587

Li, J.-L. F., Lee, W.-L., Yu, J.-Y., Hulley, G., Fetzer, E., Chen, Y.-C., & Wang, Y.-H. (2016). The impacts of precipitating hydrometeors radiative effects on land surface temperature in contemporary GCMs using satellite observations. *Journal of Geophysical Research: Atmospheres*, *121*, 67–79. https://doi.org/10.1002/2015JD023776

Li, J.-L. F., Waliser, D. E., Stephens, G., & Lee, S. (2016). Characterizing and understanding cloud ice and radiation budget biases in global climate models and reanalysis. *Meteorological Monographs*, *56*, 13.1–13.20.

Li, J.-L. F., Waliser, D. E., Stephens, G., Lee, S., L'Ecuyer, T., Kato, S., et al. (2013). Characterizing and understanding radiation budget biases in CMIP3/CMIP5 GCMs, contemporary GCM, and reanalysis. *Journal of Geophysical Research: Atmospheres*, *118*, 8166–8184. https://doi.org/10.1002/jgrd.50378

Ma, Q., Wang, K., & Wild, M. (2014). Evaluations of atmospheric downward longwave radiation from 44 coupled general circulation models of CMIP5. *Journal of Geophysical Research: Atmospheres*, *119*, 4486–4497. https://doi.org/10.1002/2013JD021427

Marshall, J. S., & Palmer, W. M. K. (1948). The distribution of raindrops with size. *Journal of Meteorology*, *5*(4), 165–166.

Mülmenstädt, J., Sourdeval, O., Delanoë, J., & Quaas, J. (2015). Frequency of occurrence of rain from liquid-, mixed-, and ice-phase clouds derived from A-Train satellite retrievals. *Geophysical Research Letters*, *42*, 6502–6509. https://doi.org/10.1002/2015GL064604

Petch, J. C. (1998). Improved radiative transfer calculations from information provided by bulk microphysical schemes. *Journal of the Atmospheric Sciences*, *55*(10), 1846–1858.

Phillips, V. T. J., & Donner, L. J. (2006). Cloud microphysics, radiation and vertical velocities in two- and three-dimensional simulations of deep convection. *Quarterly Journal of the Royal Meteorological Society*, *132*(621C), 3011–3033.

Reynolds, R. W., Smith, T. M., Liu, C., Chelton, D. B., Casey, K. S., & Schlax, M. G. (2007). Daily high-resolution-blended analyses for sea surface temperature. *Journal of Climate*, *20*(22), 5473–5496.

Savijärvi, H., Arola, A., & Räisänen, P. (1997). Short-wave optical properties of precipitating water clouds. *Quarterly Journal of the Royal Meteorological Society*, *123*(540), 883–899.

Savijärvi, H., & Räisänen, P. (1998). Long-wave optical properties of water clouds and rain. *Tellus A: Dynamic Meteorology and Oceanography*, *50*(1), 1–11.

Slingo, A., & Schrecker, H. M. (1982). On the shortwave radiative properties of stratiform water clouds. *Quarterly Journal of the Royal Meteorological Society*, *108*(456), 407–426.

Stephens, G. L., Li, J., Wild, M., Clayson, C. A., Loeb, N., Kato, S., et al. (2012). An update on Earth's energy balance in light of the latest global observations. *Nature Geoscience*, *5*(10), 691–696.

Tang, G., Yang, P., Stegmann, P. G., Panetta, R. L., Tsang, L., & Johnson, B. (2017). Effect of particle shape, density, and inhomogeneity on the microwave optical properties of graupel and hailstones. *IEEE Transactions on Geoscience and Remote Sensing*, *55*(11), 6366–6378.

Tao, W.-K., Lang, S., Zeng, X., Li, X., Matsui, T., Mohr, K., et al. (2014). The Goddard Cumulus Ensemble model (GCE): Improvements and applications for studying precipitation processes. *Atmospheric Research*, *143*, 392–424.

Tao, W.-K., Lau, W., Simpson, J., Chern, J.-D., Atlas, R., Randall, D., et al. (2009). A multiscale modeling system: Developments, applications, and critical issues. *Bulletin of the American Meteorological Society*, *90*(4), 515–534.

Tao, W.-K., Simpson, J., Baker, D., Braun, S., Chou, M.-D., Ferrier, B., et al. (2003). Microphysics, radiation and surface processes in the Goddard Cumulus Ensemble (GCE) model. *Meteorology and Atmospheric Physics*, *82*(1-4), 97–137.

Tao, W.-K., Wu, D., Lang, S., Chern, J.-D., Peters-Lidard, C., Fridlind, A., & Matsui, T. (2016). High-resolution NU-WRF simulations of a deep convective-precipitation system during MC3E: Further improvements and comparisons between Goddard microphysics schemes and observations. *Journal of Geophysical Research: Atmospheres*, *121*, 1278–1305. https://doi.org/10.1002/2015JD023986

Waliser, D. E., Li, J.-L. F., L'Ecuyer, T. S., & Chen, W.-T. (2011). The impact of precipitating ice and snow on the radiation balance in global climate models. *Geophysical Research Letters*, *38*, L06802. https://doi.org/10.1029/2010GL046478

Warren, S. G. (1984). Optical constants of ice from the ultraviolet to the microwave. *Applied Optics*, *23*(8), 1206–1225.

Wilcox, E. M. (2012). Direct and semi-direct radiative forcing of smoke aerosols over clouds. *Atmospheric Chemistry and Physics*, *12*(1), 139–149.

Wild, M., Folini, D., Hakuba, M. Z., Schär, C., Seneviratne, S. I., Kato, S., et al. (2014). The energy balance over land and oceans: An assessment based on direct observations and CMIP5 climate models. *Climate Dynamics*, *44*(11-12), 3393–3429.

Xu, K.-M., & Randall, D. A. (1995). Impact of interactive radiative transfer on the macroscopic behavior of cumulus ensembles. Part I: Radiation parameterization and sensitivity tests. *Journal of the Atmospheric Sciences*, *52*(7), 785–799.